JMEPEG (2011) 20:1114–1120
DOI: 10.1007/s11665-010-9753-7

©ASM International
1059-9495/$19.00

Modeling the Evolution of Stresses Induced by Corrosion Damage in Metals

Ramana M. Pidaparti and Ronak R. Patel

(Submitted October 13, 2009; in revised form June 1, 2010)

Corrosion is one of the most damaging mechanisms in aluminum alloys commonly used in aerospace engineering structures. Cracks usually initiate from the pits/defects, and currently, there are no measurement probes that can estimate the stress environment around corrosion pits. In this article, a systematic study is conducted to investigate the evolution of corrosion-damage-induced stresses in aluminum alloy 2024-T3 as a function of time. Corrosion experiments were conducted on a metal sample under controlled electrochemical conditions and the surfaces were imaged using AFM techniques. A computational procedure was developed to investigate the stresses resulting from corrosion damage/pits using the AFM image, CAD, and finite element analysis. Analysis was also carried out on corroded specimens under bending and tension loadings in order to see how the loading affects the induced stresses. The results indicated that the stress distribution and levels on the corroded surface varied due to irregularities and randomness in the metal sample. The results also indicated that the stress initially increases and reaches a plateau with increasing corrosion time and may be responsible for failure (crack initiation) of the metals.

Keywords AFM, aluminum alloys, finite element analysis, pit-induced corrosion, stresses

1. Introduction

Corrosion is the degradation of the metallic structure at its surface through chemical reaction of the metal with the environment. Aluminum alloys such as 2024-T3 and 7075-T6 are used in many aerospace structures due to their high strength, low density, and high resistance to corrosion. These alloys are subjected to pitting corrosion and film forming corrosion due to the presence of numerous constituent particles, which play an important role in corrosion. Corrosion pits generally initiate due to some chemical or physical heterogeneity at the surface, such as inclusions, second phase particles, or dislocations in aluminum alloys (Ref 1-3). Techniques such as optical microscopy, scanning electron microscopy (SEM), atomic force microscopy (AFM), and transmission electron microscopy (TEM) have been used to better understand particle-induced pitting corrosion in aluminum alloys (Ref 4). Corrosion mechanisms including pitting depend on the material composition, electrolyte, and other environmental conditions (Ref 1-3).

Cracks usually initiate from the corrosion damage sites in the material. Under the interaction of cyclic load and the corrosive environment, cyclic loading facilitates the pitting process, and corrosion pits, acting as geometrical discontinuities, lead to crack initiation and propagation and then final failure (Ref 5-10). Corrosion can lead to accelerated failure of structural components under fatigue loading conditions. Understanding and predicting corrosion damage is very important for assessing the structural integrity of materials and structures.

To predict the spatial distribution of potential or current on the metal surface and to quantify the corrosion rate, several local probe techniques based on electrochemical measurements have been studied. These include scanning reference electrode technique (SRET), scanning vibrating electrode technique (SVET), and localized impedance spectroscopy (LEIS) (Ref 11-14), among others. Also, to quantitatively evaluate the local corrosion damage on metal specimens, various physical probes such as SEM, AFM, and STM based on near field microscopy have been applied (Ref 15) in the literature. There are no measurement probes that can estimate the stress environment around corrosion pits. Usually, high stress regions around the corrosion pits are considered to be responsible for stress corrosion cracking. The goal of our study is aimed at developing a combined experimental and computational modeling approach to comprehensively investigate the evolution of stresses due to the corrosion damage process. The developed approach might be useful for predicting the stresses responsible for crack initiation in aluminum alloys. The approach was briefly discussed and preliminary results were presented in Ref 16. However, further investigation is necessary to quantify the evolution of corrosion-pit-induced stresses under different loadings during the corrosion process.

The objective of this study is to systematically investigate the evolution of corrosion-damage-induced stresses in aluminum alloy 2024-T3 as a function of time and relate this information to material loss due to corrosion. Corrosion experiments were conducted on metal samples under controlled electrochemical conditions and their surfaces were imaged using AFM techniques. A computational procedure was developed to investigate the stresses resulting from corrosion damage/pits using the AFM image, CAD, and finite element

---

Ramana M. Pidaparti and **Ronak R. Patel**, Department of Mechanical Engineering, Virginia Commonwealth University, 401 West Main Street, Richmond, VA. Contact e-mail: rmpidaparti@vcu.edu.

analysis. Analysis was also carried out on corroded specimens under bending and tension loadings in order to see how the loading affects the induced stresses.

2. Experiments

2.1 Sample Preparation

The material used was an aluminum alloy 2024-T3, which was received in sheet form (12″ × 12″) with a nominal thickness of 1.5 mm. Initially, the specimens were first inspected visually and then with an optical microscope for any imperfections on the surface. If the specimen had any imperfections, it was not included in the study. Surface imperfections can act as a source of initiation of corrosion due to low corrosion resistance and may also create an artifact in the corrosion process. After selection of the specimens with no imperfection on the surface, the specimens were prepared for corrosion testing.

The selected specimens were grounded with 200, 500, 800, and 1200 grid emery papers. Initially, the specimens were grounded with 200 grid emery papers at 60 rpm for about 2 min. Water was used as a coolant to remove the waste material. This process was repeated with 500 and 800 grid papers. Next, the specimens were ground with 1200 grid emery paper at 120 rpm for about 4 min to ensure that no sharp edges are left on the surface. After the grinding is completed, the specimens were washed with fresh water and then dipped in the ethanol solution for complete removal of the waste from the grounded surface. The specimens were then polished with 6 and 1 μm diamond spray polishing plates. The polishing plates were kept at 120 rpm and polished for 4 min on both plates. After polishing, the specimens were washed with fresh water and taken for further cleaning.

After the specimens are polished, they are cleaned using the ultrasonic cleaning machine. The specimens were initially dipped in a diluted acetone solution, then placed in a 70% ethanol solution and finally in distilled water for 15 min each. After the cleaning process, the specimens were removed from the ultrasonic cleaning machine and allowed to dry under air. Once the specimens are completely dry, an area of 1 × 1 mm is selected for corrosion study and the rest of area on the specimens was coated with paint. The coating ensures that there is no corrosion on the sample surface except the selected region for the corrosion studies.

2.2 Experimental Protocol

Initially, different specimens were considered for different time intervals in a 5 M NaCl corrosive environment, but the results from optical imaging appeared to be very random. Corrosion varied from one specimen to another in an identical corrosive environment. This effect may be due to changes in the metallurgical properties of the specimen material. As we know that corrosion resistance is dependent on many factors, this resistance varies even in the same material. To avoid the randomness in the results, the same specimen was used to investigate the extent of corrosion as our goal is to systematically study the corrosion with respect to time.

The exclusion of different specimens under different corrosion times helped to eliminate randomness in the optical imaging but severe corrosion was observed during the 15-min interval of the corrosion process. This effect was due to the highly corrosive environment formed by the 5 M NaCl electrolyte solution. It was therefore very difficult to predict the effect of corrosion with respect to time. To avoid rapid corrosion in the material, the corrosive environment was diluted to 2 M NaCl solution in the electrochemical cell. The electrochemical cell consists of an electrolyte and three electrodes; working, reference, and auxiliary electrodes as shown in Fig. 1. The sample which had to corrode was used as working electrode. Reference electrode which is a platinum wire was used to measure the working electrode potential. A reference electrode should have a constant electrochemical potential as long as no current flows through it. The auxiliary electrode is a conductor that completes the cell circuitry. In this cell, the auxiliary electrode used was graphite. The electrolyte creates the environment for corrosion by providing ions. Ideally the electrode which is supposed to be corroded is kept as an anode, and potential voltage is supplied to cell in order to initiates the corrosion process.

An electrochemical cell setup (GAMRY) was used for corroding the specimen under 2 M NaCl electrolyte solution and a voltage of -0.63V was applied. A reference or set point was used when comparing the corroded images at different times. The corroded specimen was scanned by AFM to obtain the pit profile after corroding for a specified time. The specimen was corroded at intervals of 15 min as shown in Fig. 1. To predict the trend of corrosion, the scan size area and height were kept constant so that they can be comparable with respect to time. The rate of corrosion is proportional to the rate of electrons transferred between the electrode and electrolyte. The current (I_{corr}) flowing through the electrochemical cell is

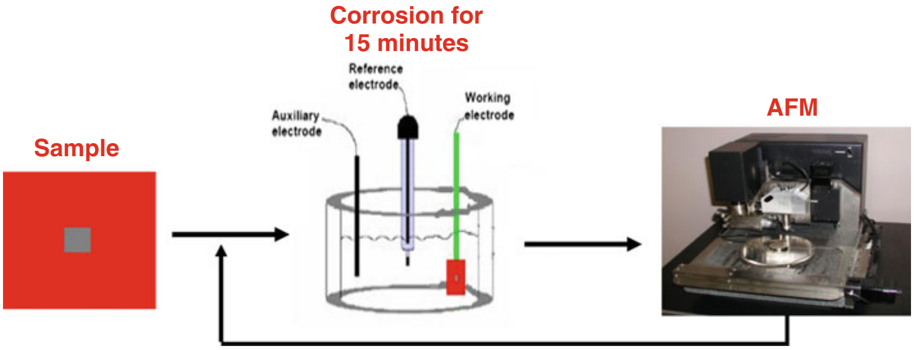

Fig. 1 An overview of experimental protocol for investigating the corrosion pit process systematically

measured and using the Faraday's law, and the corrosion rate (CR) can be calculated as

$$\mathrm{CR} = I_{\mathrm{corr}}\, K\, \mathrm{EW}/(\rho A),$$

where I_{corr} is current which is obtained from Gamry Electrochemical setup, K is a constant, in this case 3272 mm/(amp*cm*year), EW is the equivalent weight of the metal (in g), ρ is density in g/cm^2, and A is area in cm^2. Using the above equation, the CR as a function of time are obtained for AA2024 alloys.

3. Stress Analysis

The stress analysis procedure is shown in Fig. 2. First the intended AFM image is cropped and NURB modeling software such as Rhinoceros (Ref 17) is used to generate a 3-D surface from a height-field image. CAD software (Ref 18) is used to create a solid model from a 3-D surface. ANSYS software (Ref 19) is used to perform a finite element analysis on the solid model to predict the induced stress on the surface under different types of loading.

When the model is imported in ANSYS software, a visual check is performed to make sure that the model has the same dimensions as in the AFM image and if not, then the model is scaled accordingly. Tetrahedral elements were used to perform stress analysis on the model. Initially, a hexahedral element was used as its accuracy is higher than that of tetrahedral element but the mesh failed as the model surface became rougher. A tetrahedral element was therefore used for all models of AA2024 specimens for different corrosion times. Structural properties like modulus of elasticity (E) and Poisson's ratio (γ) are specified for the all the models of AA2024 specimen (E = 72 GPa and γ = 0.3). Linear isotropic structural analysis is performed by applying the boundary conditions on the model.

The loading conditions for bending and tension loading are shown in Fig. 3. A uniform pressure of 1 MPa is applied along the center line on the bottom of the model. The top four corners are fixed for bending loading. For tension loading, the boundary condition is achieved by applying zero displacement to one face (area) in $-X$ direction, and applying a 1 MPa on the face in the +X direction. The finite element stress analysis is performed on the model after applying the appropriate boundary condition for the particular type of loading.

Convergence test was performed on the finite element model in order to get accurate stress results. The stress results of convergence test performed on the finite element model at time t = 45 min under bending are considered. Seven different finite element models were considered with varying elements from 45,000 to 450,000 finite elements. As the number of mesh elements is increased, the maximum stress induced also increased and soon reached a plateau. When the maximum induced stress reaches a plateau, it indicates that the number of mesh elements has been optimized and any further increase in the number of elements has a negligible effect on the maximum induced stress. In most of the models, the solution optimized when the number of elements were in the 350,000-450,000 range, with a stress accuracy of 1% was achieved. After the convergence test, simulations were carried out for all specimens to investigate the effect of corrosion time on von-Mises stresses at the maximum pit depth of the corroded specimens. The converged meshes for both bending and tension loadings are shown in Fig. 3.

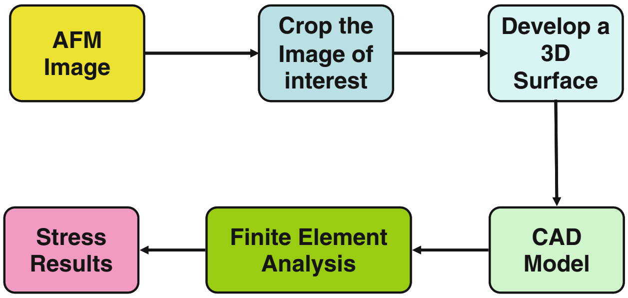

Fig. 2 An overview of the process for the prediction of corrosion-pit-induced stresses from AFM images

4. Results and Discussion

4.1 Experiments

The results of CR obtained from the experimental data are shown in Fig. 4. It can be observed from Fig. 4 that the CR increases sharply as the AA2024 sample is first corroded and CR decreases slightly due to passivity of the material. However, as time increases, the CR increases and soon reaches its maximum value and then there is a decrease in CR due to saturation. In order to predict the trend in corrosion rate, two-order polynomial regression was used. The results in the prediction trend indicate that the CR increases as the corrosion time is increased and soon reaches a plateau.

Table 1 summarizes the findings from AFM images of corroded specimen at different times. It is interesting to see pits initiating and growing and depositing corrosion products with

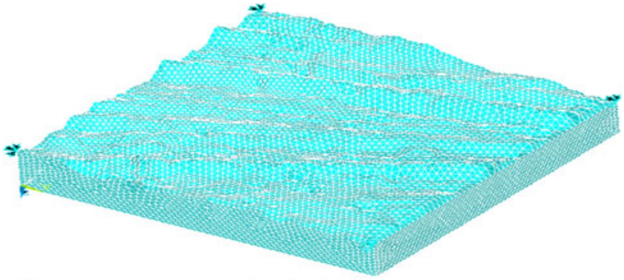

(a) Bending loading

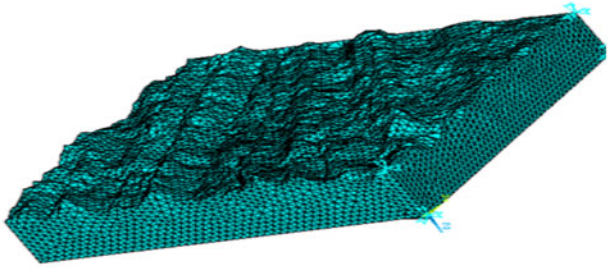

(b) Tension loading

Fig. 3 Finite element models under bending and tension loadings considered

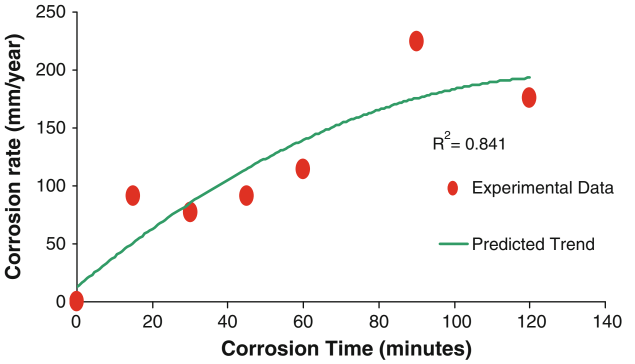

Fig. 4 Variation of corrosion rate with time for the metal specimens considered under 2 M NaCl electrolyte solution at −0.63 V

Table 1 Surface characteristics observed through AFM images of corroded specimen (see Fig. 6)

Time (min)	AFM surface image characteristics
15	Some regions of the surface seem to be corroded uniformly. The surface roughness increases sharply by 47.1% and wavy profile is observed with few long groove type of pits
30	Growth of wavy pattern and pit enlargement is observed. The surface roughness has increased by 14.6%
45	Depositions of oxides on the surface increases and some pits are covered with corrosion products. Three pits are observed at this particular time and there is negligible increase in surface roughness
60	Few pits are covered with oxides and the rest of pits are expanded in size. Wavy kind of profile is observed and the surface roughness is increased by 21% due to accumulation of oxides
90	Few bumps are observed on the surface and pits are narrowed due to oxide depositions. However, the increase in surface roughness was negligible
120	Random deposition of oxide is observed over entire area due to few pits and bumps are observed and the surface roughness has increased by 23.9%

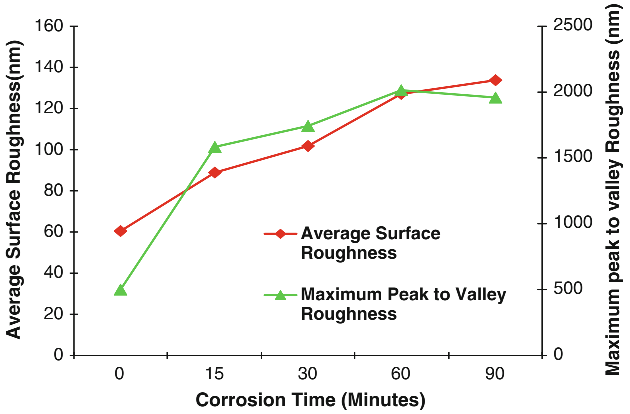

Fig. 5 Experimentally measured surface roughness through AFM image of corroded surface of 2024-T3 aluminum specimen at various times of corrosion

increasing time. The surface morphology characteristics obtained from AFM imaging software are shown in Fig. 5. The average surface roughness of the sample increased sharply by 47.1% when the specimen was initially corroded for 15 min. Under further corrosion, the increase in surface roughness seemed to decline due to saturation of the number of irregularities on the surface. There was an increase in surface roughness due to accumulation of the oxides on the surface. Similar trend was observed on the maximum peak to valley roughness ($R_{\max}$) as the corrosion time increased.

4.2 Stress Analysis

Based on the converged finite element models, the stress analysis is carried out on specimen for various corrosion times. Figure 6 shows the von-Mises stress distributions on the model surface obtained from the finite element analysis of the corroded specimen at 15 and 90 min under bending. The results of stress distributions at corrosion times of 30 and 60 min are presented in Pidaparti and Patel (Ref 16). For the sample corroded for $t = 15$ min, the maximum von-Mises stress is at 22.5 MPa and it is induced at the pit located on the side of the model surface. The surfaces which are at a higher height due to bumps formed from the accumulation of the oxides have lower induced stress regions on them, while the long pit like structures have higher induced stress regions. The induced stress changes as the height is varied on those bumps and pits. As shown in Fig. 6, at total corrosion time, the accumulation of the corrosion product and the average surface roughness continue to increase. There are bumpy kinds of structures formed on the surface due to increased corrosion. The deposition of the corrosion product on the corroded surface seemed to increase, but is not uniform. For corrosion time $t = 90$ min, the stress distribution observed is similar to that obtained in (Ref 16), but the surface roughness has increased and so has the maximum induced stress. However, the increases in induced maximum stress decreased as the time increased.

Figure 7 shows the correlation of maximum von-Mises stress as a function of corrosion time. It can be seen that as the corrosion time increases, the pit stresses increase and reach a plateau. Initially, the stress increases faster due to sharp pits and then becomes flat due to the blunting of the pits. There is a stress increase of 80% within the first 30 min, and the increase is about 6% when the sample is corroded from 30 to 60 min. After 60 min of total corrosion time, there is a negligible increase of 2% in maximum stress when corroded further. This suggests that further growth of oxide layers does not increase the maximum stress. However, the strength of the oxide layers is less than that of the sample and it might result in failure under these loadings. The failure of the oxide layer was not considered in this particular analysis and may result in formation of more pits or enlargement of the pit which further increases the maximum stress on the sample surface. The pit stress level of 30 MPa obtained from this study is of a reasonable magnitude to initiate a crack, since the facture toughness of AA2024 alloys is in the range of 26-37 MPa $\mathrm{m}^{1/2}$ (Ref 16).

Figure 8 shows the von-Mises stress distribution on the model surface obtained from the finite element analysis of the corroded AA2024 sample at different times under tension loading. As seen from Fig. 8(a), when the sample is not corroded, the induced stress distribution on the surface seems to be uniform. The maximum stress induced is 1.04 MPa in the regions near the face, where the unit pressure load was applied.

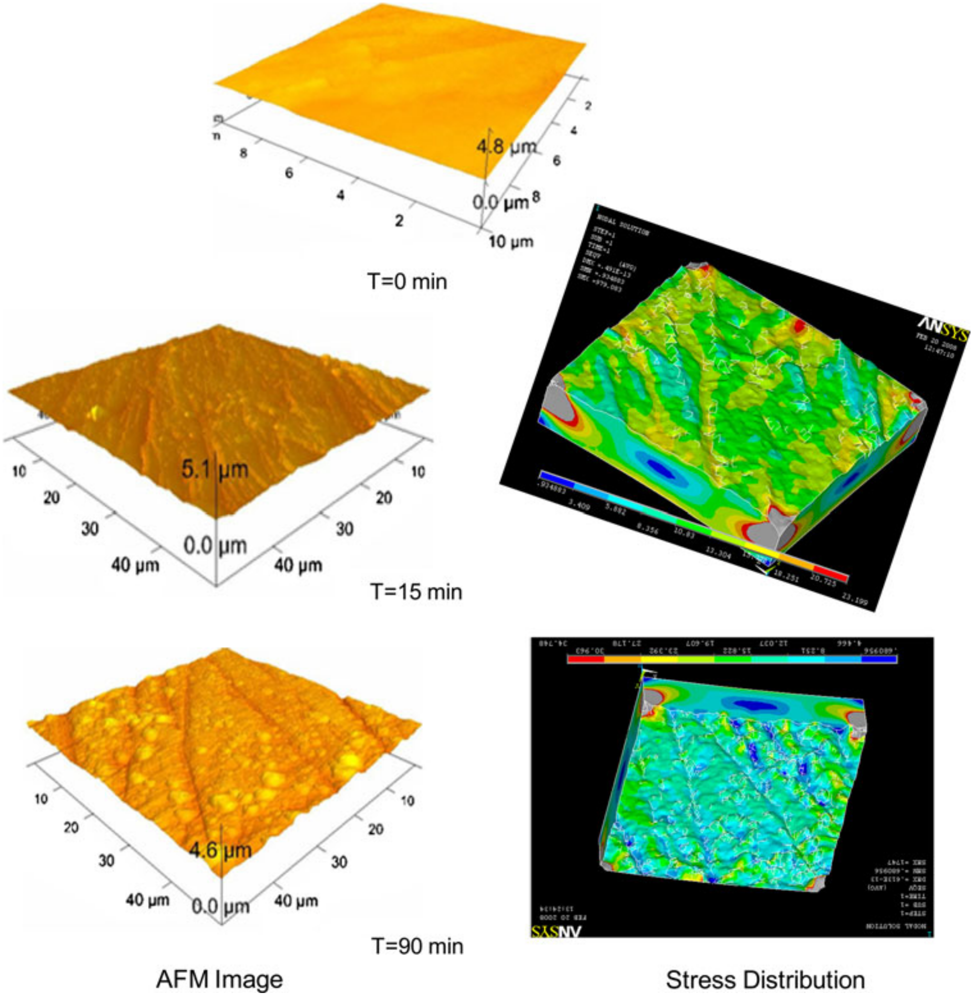

Fig. 6 AFM images at different times of corrosion

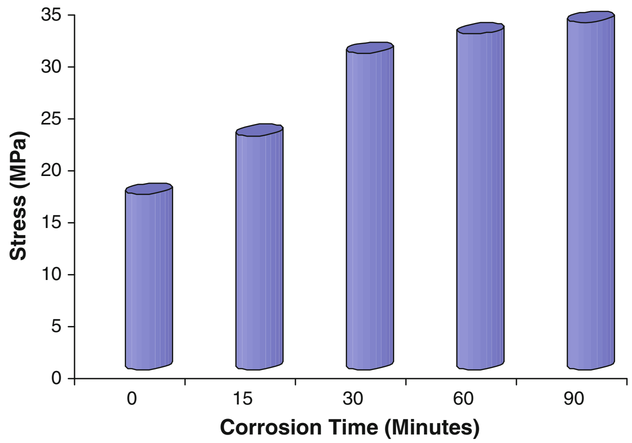

Fig. 7 Maximum von-Mises stress on the model surface at different times of corrosion under bending loading

The region near the fixed displacement corners was ignored from the study as it induced more stress due to restrictions of the displacement. Low stress region are generally formed near the fixed corners. At corrosion time t = 15 min (Fig. 8b), due to deposition of the oxide on the surface, an uneven induced stress distribution was observed. The deposition of oxides has created a few bumps, grooves, and pits on the surface which has increased the surface roughness of the model. The bumpy regions shows less stress induced under tension loading, and regions with groove and pits which are lower in height seem to have induced high stress region within them. The maximum stress of 1.52 MPa is observed at the maximum pit size.

As the corrosion time is further increased (Fig. 8c-e), there is an increase in deposition of the oxide which has change the size and shape of the bumps, grooves, and pits on the surface. There is a change in stress regions due to this change in size and shape of the irregularities on the surface. It can therefore be predicted that the stress distribution on the model surface is dependent on the height and shape of the irregularities on it. Similar stress distributions are observed for all corrosion times when the specimen is further corroded. Low stress regions are observed on the regions which are at a higher height as compared to the neighboring regions, and high stress regions are observed on the regions which are at a lower height. The grooves on the surface which is less corroded or un-corroded are also considered similar to pits as these regions induce high stress regions within them. However, maximum stresses are induced on the pits which are at maximum pit depth.

Figure 9 shows the maximum von-Mises stress predicted for AA2024 at different corrosion times under tensile loading.

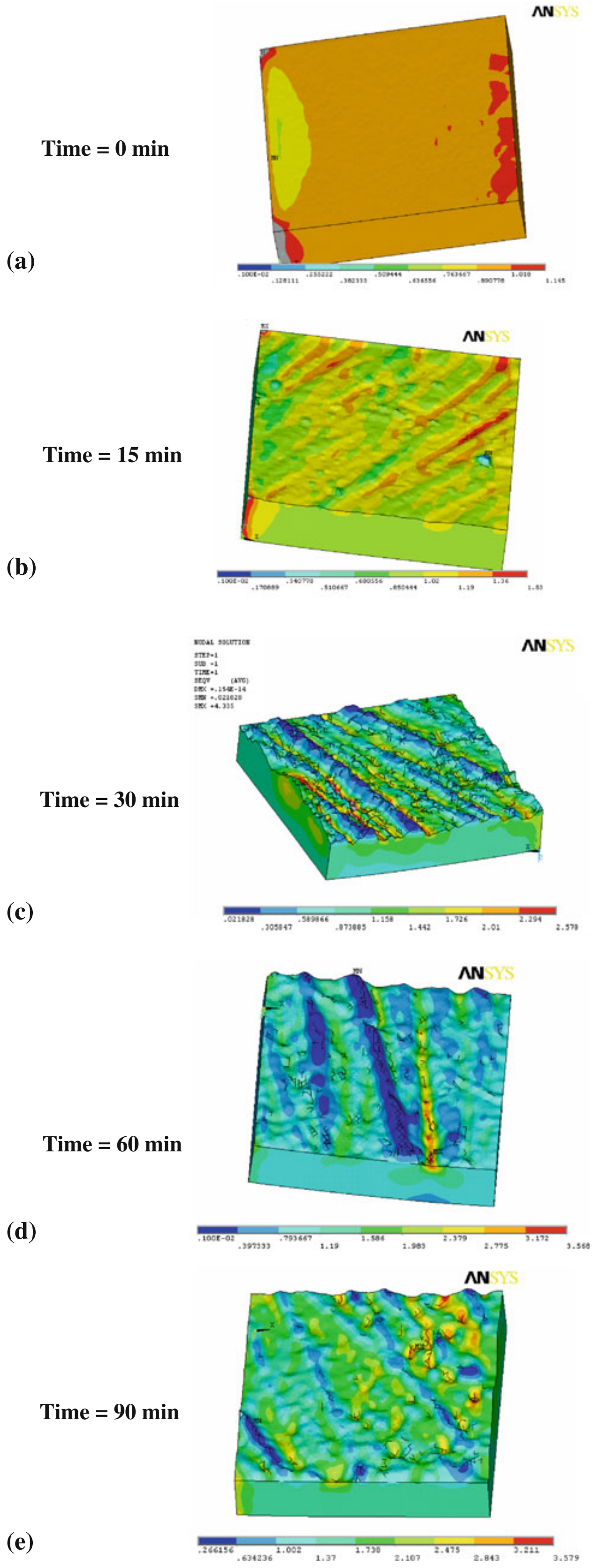

Fig. 8 von-Mises stress distributions on the model surface at different times of corrosion under tension loading

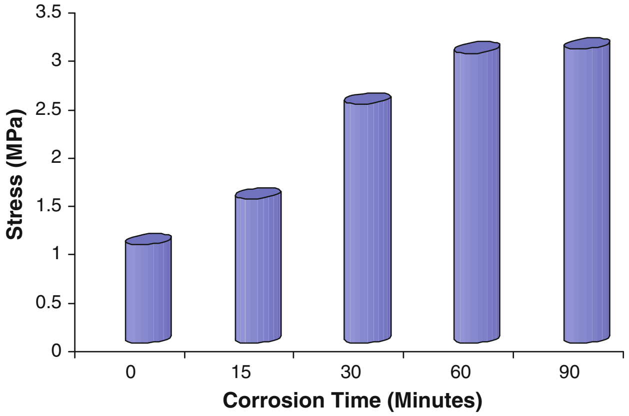

Fig. 9 Maximum von-Mises stress on the model surface at different times of corrosion under tension loading

Initially, when the sample is not corroded, the maximum stress induced is close to 1 MPa, same as the stress applied. When the sample is corroded further for 15 min there was an increase of 31.6% in maximum stress. This increase was due to increase in surface roughness because the pits and bumps have formed on the surface. During the time interval 15-30 min there was further increase in maximum stress by 35.6%. The increase in maximum stress on further corrosion seems to be declining due to saturation in formation of the irregularities on the surface. At *t* = 60 min, there was a 29.32% increase in maximum stress due to increase in deposition of the oxides which have increased the relative depth of the pit. However, at time *t* = 90 min, the increase in maximum stress was reduced to 6% due to saturation of irregularities on the surface. It appears that maximum stress has reached a plateau and there will be negligible increase in maximum stress with further corrosion. Overall, the maximum stress increases as the corrosion time is increased and then it will reach a plateau. The tensile loading can lead to breakdown of the oxide layers on the sample and can even expedite the process of pit growth. The results presented in Fig. 6-9 illustrate that the pit-induced stresses vary not only with corrosion time, but also the type of loading they are subjected to.

5. Conclusions

Experimental measurements were conducted on aluminum 2024-T3 specimens to observe the corrosion degradation and initiation and growth of pits. AFM of corroded specimen was carried out to observe how the pits grow and progress with time. An analysis procedure was developed using CAD and finite element software to predict stresses due to corrosion pits. The stress results obtained under bending indicate that the stresses increase by 80% within the first 30 min of corrosion and then increase by about 6% from 30 to 60 min and reach a plateau. The magnitude of stress results is higher in bending in comparison to tension loading. From the corrosion-damage-induced stress predictions, it is possible to estimate the initiation of cracks, from which the failure life of the material can be determined.

Acknowledgments

The authors thank the U. S. National Science Foundation for sponsoring this research through grant DMR-0505039.

References

1. P. Marcus and J. Oudar, Ed., *Corrosion Mechanisms in Theory and Practice*, Marcel Dekker, Inc., New York, 1995
2. L.L. Shreir, R.A. Jarman, and C.T. Burstein, Ed., *Corrosion-Metal/Environmental Reactions*, 3rd ed., Butterworth & Heinemann Ltd, Oxford, 1994
3. H.H. Strehblow, Mechanisms of Pitting Corrosion, *Corrosion Mechanisms in Theory and Practice*, P. Marcus and J. Oudar, Ed., Marcel Dekker, Inc., New York, 1995, p 201–238
4. R.P. Wei, C.M. Liao, and M. Gao, A Transmission Electron Microscopy Study of 7075-T6 and 2024-T3 Aluminum Alloys, *Metallurgical and Materials Transactions A*, 1998, **29A**, p 1153–1160
5. K. Jones and D.W. Hoeppner, Prior Corrosion and Fatigue of 2024-T3 Aluminum Alloy, *Corros. Sci.*, 2006, **48**, p 3109–3122
6. D.W. Hoeppner, *Fatigue Mechanisms STP*, Vol 675, American Society for Testing and Materials (ASTM), Philadelphia, PA, 1979, p 841–870
7. G.T. Burstein, C. Liu, R.M. Souto, and S.P. Vines, Origins of Pitting Corrosion, *Corros. Eng. Sci. Technol.*, 2004, **39**, p 25–30
8. G.N. Frantiziskonis, L.B. Simon, J. Woo, and T.E. Matikas, Multiscale Characterization of Pitting Corrosion and Application to an Aluminum Alloy, *Eur. J. Mech. A Solids*, 2000, **19**, p 309–318
9. S.I. Rokhlin, J.Y. Kim, H. Nagy, and B. Zoofan, Effect of Pitting Corrosion on Fatigue Crack Initiation and Fatigue Life, *Eng. Fract. Mech.*, 1999, **2**, p 425–444
10. S. Ishihara, S. Saka, Z.Y. Nan, T. Goshima, and S. Sunada, Prediction of Corrosion Fatigue Lives of Aluminum Alloy on the Basis of Corrosion Pit Growth Law, *Fatig. Fract. Eng. Mater. Struct.*, 2006, **29**, p 472–480
11. H.S. Isaacs, Initiation of Stress Corrosion Cracking of Sensitized Type 304 Stainless Steel in Ductile Thiosulfate Solution, *J. Electrochem. Soc.*, 1988, **135**, p 2180–2183
12. T. Suter and H. Bohni, A New Microelectrochemical Method to Study Pit Initiation on Stainless Steels, *Electrochim. Acta*, 1997, **42**, p 275–328
13. R. Oltra and V. Vignal, Recent Advances in Local Probe Techniques in Corrosion Research—Analysis of the Role of Stress on Pitting Sensitivity, *Corros. Sci.*, 2007, **49**, p 158–165
14. C.H. Paik and R.C. Alkire, Role of Sulfide Inclusions on Localized Corrosion of Ni200 in NaCl Solutions, *J. Electrochem. Soc.*, 2001, **148**, p B276–B281
15. P. Schmutz and G.S. Frankel, Corrosion Study of AA2024-T3 by Scanning Kelvin Probe Force Microscopy and In Situ Atomic Force Microscopy Scratching, *J. Electrochem. Soc.*, 1998, **145**, p 2295–2306
16. R.M. Pidaparti and R.R. Patel, Correlation Between Corrosion Pits and Stresses in Al Alloys, *Mater. Lett.*, 2008, **62**(30), p 4497–4499
17. Rhinoceros 4.0, *Rhino 4.0 Tutorial*, McNeel North America, Seattle, WA, 2007
18. SolidWorks, *SolidWorks Tutorial*, SolidWorks Corporation, Concord, MA, 2007
19. ANSYS 11.0, *ANSYS Tutorial*, ANSYS Inc., Canonsburg, PA, 2007